MDPI

Article

In Situ Mineralogical Constraints on Magmatic Process for Porphyry Deposits in the Upper Crust: A Case from Tongchang–Chang'anchong Porphyry Deposits, SW China

Zixuan Wang [1], Yuanchuan Zheng [2,*], Bo Xu [1,2,3,*], Yang Shen [4] and Lu Wang [2]

[1] School of Gemology, China University of Geosciences Beijing, Beijing 100083, China
[2] State Key Laboratory of Geological Processes and Mineral Resources, China University of Geosciences, Beijing 100083, China
[3] The Beijing SHRIMP Center, Chinese Academy of Geological Sciences, Beijing 100037, China
[4] State Key Laboratory of Marine Geology, and School of Ocean and Earth Science, Tongji University, Shanghai 200092, China
* Correspondence: zhengyuanchuan@gmail.com (Y.Z.); bo.xu@cugb.edu.cn (B.X.)

Abstract: The magmatic process within upper crust encompasses various contents such as the transition between magmatic and hydrothermal systems and changes in oxygen fugacity (fO_2), which ultimately play key roles in the formation of porphyry Cu deposits (PCDs). However, tracing these magmatic processes, especially in porphyry systems, is not an easy task. This study reported the detailed process of magmatic fluid exsolution and systematical variation of magmatic fO_2 within the upper crust of a Tongchang–Chang'anchong porphyry Cu deposit, based on detailed investigations of mineral crystallization sequences and compositional features of the minerals in the fertile porphyries. Results indicate that the fertile porphyries show a high initial fO_2, with ΔFMQ $\geq$ +3.0 (ΔFMQ is the deviation of logfO_2 from the fayalite–magnetite–quartz (FMQ) buffer). The magmatic fO_2 (ΔFMQ) continued to decrease to ~+2 until fluid exsolution occurred at ~790 °C due to wall-rock contamination. The magmatic fluid exsolution process caused a temporary increase in the fO_2 (to ΔFMQ = ~+3.4). The high magmatic fO_2 during this process (790–750 °C) resulted in a higher content of ore-forming materials in the exsolved magmatic fluid. When the temperature dropped below 750 °C, the magmatic fO_2 began to continuously decrease and eventually reached ΔFMQ = ~+0.6. The lower magmatic fO_2 hindered the further migration of ore-forming materials through the exsolved fluid during this process (< 750 °C). Results of this study indicate that the initial magma during the upper crustal magmatic process of PCDs generally has a high fO_2, and the contamination of reduced components can significantly decrease the magmatic fO_2. The early magmatic fluid exsolution process can maintain a high magmatic fO_2 condition, thereby efficiently extracting ore-forming minerals and producing ore-forming fluids, which is the key to the formation of PCDs. The latter continuous decrease in magmatic fO_2 during the fluid exsolution process may be the reason preventing the Tongchang–Chang'anchong porphyry Cu deposit to form a giant PCD.

Keywords: porphyry deposit; oxygen fugacity (fO_2); fractional crystallization; fluid exsolution; magmatic process

1. Introduction

Porphyry Cu deposits (PCDs) are presently the main source of Cu (~75%) and a substantial source of Au (~20%) around the world [1]. The ore bodies of PCDs predominantly occur at shallow crustal level around dike-like porphyries, e.g., [2,3]. It is well known that PCDs are usually associated with oxidized and volatile-rich magmas within shallow magma chambers, e.g., [3–9]. The magmatic–hydrothermal processes occurring in shallow magma chambers can play an essential role in supplying enough ore-forming fluids to generate the hydrothermal system [10–12]. The detailed properties of volatile components

and oxygen fugacity (fO_2) directly control the fluid exsolution and the metals budget in the magmatic fluid during the magmatic–hydrothermal processes [12,13]. As a result, tracking the volatile components and fO_2 throughout the magma phases is crucial for our understanding of the formation of PCDs.

Minerals in cogenetic ore-bearing intrusions are sensitive to various factors of the magma processes, such as fO_2, temperature and melt composition. As a result, they serve as a valuable tool for estimating the crystallization conditions and compositions of their equilibrium melt phase, e.g., [14–22]. The utilization of multiple minerals is more effective in characterizing the comprehensive magmatic process, as different minerals undergo crystallization at different stages. Moreover, the implementation of mineral thermobarometers can delineate the alteration of fO_2 and volatile components during the magmatic evolution and magmatic–hydrothermal processes, e.g., [19,23–25]. This approach allows for a deeper understanding of shallow magma processes and their impact on porphyritic mineralization. However, few studies have tried to trace the complete magmatic evolution and magmatic–hydrothermal processes within a single magma system.

Here, we aim at decoding the volatile components and fO_2 records of amphibole, biotite, zircon and apatite from the fertile porphyries associated with the Tongchang–Chang'anchong porphyry Cu (–Mo) deposits. This porphyry system mainly produces Cu and Mo and is closely related to the Chang'an Au system, which represents an opportunity to understand the evolution of volatiles and fO_2 within upper-crustal magmatic process of PCDs and try to identify the key point leading to the formation of the porphyritic mineralization.

2. Geological Setting

The Jinshajiang–Red River belt, trending in a northwestern direction, is a crustal-scale strike-slip fault zone situated between the South China and Indochina–Simao blocks (Figure 1). This belt was formed as a result of the eastern Paleo–Tethyan ocean closure during the Middle to Late Triassic [26]. Subsequently, the belt underwent Cenozoic reactivation and generated the Eocene–Oligocene (43–32 Ma) magma belt due to post India–Asia collisional tectonics (Figure 1) [27–32]. The Eocene–Oligocene magma belt within the Jinshajiang–Red River belt hosts a large number of important PCDs, which are primarily associated with felsic porphyry exhibiting adakitic affinity [33–39].

The northern segment of the Jinshajiang–Red River belt is represented by the Yulong porphyry Cu–Mo belt (comprising the Narigongma, Baomai, Yulong, Zhanaga, Mangzong, Malasongduo, and Duoxiasongduo from north to south), hosting total ~9 Mt Cu and ~0.8 Mt Mo resources, respectively [33,40,41]. Molybdenite Re–Os dating of the Cu mineralization (~42–36 Ma) suggested that the mineralization was largely coeval with the emplacement of monzogranite and granite porphyries (~44–36 Ma) [40,42,43]. The southern segment of the belt is represented by the Ailaoshan–Red River porphyry Au–Cu–Mo belt (comprising the Beiya, Yao'an, Machangqing, Habo and Tongchang–Chang'anchong deposits). These deposits together have a total Au metal endowment of >330 t and Cu metal resource of ~1.4 Mt, with ~0.06 Mt Mo reserves [34,36,42,44–46]. The mineralization (molybdenite Re–Os dating: ~37–33 Ma) is regarded to be associated with monzogranite and granite, plus minor syenite and quartz syenite (~38–36 Ma) [32,35,42,47,48].
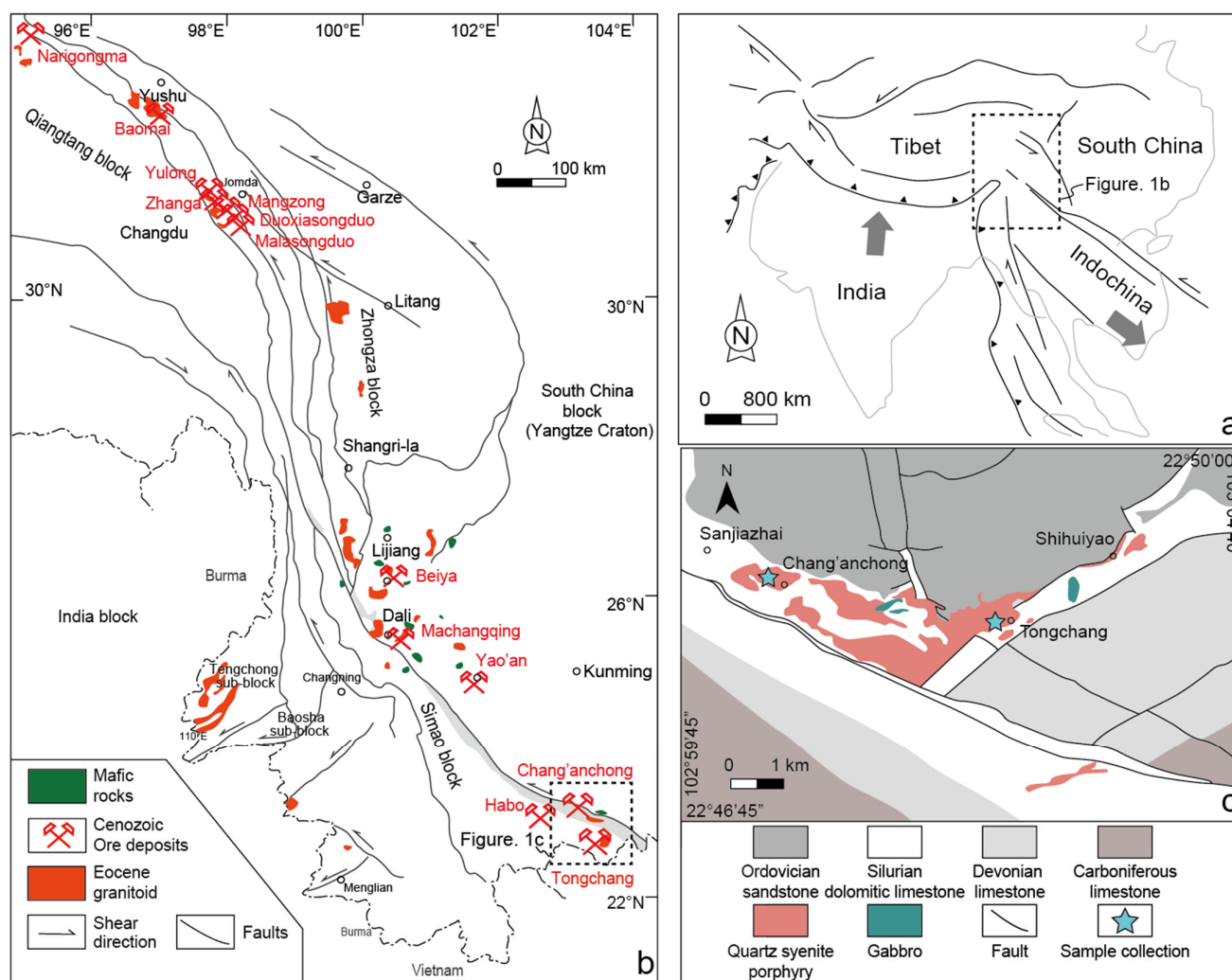
Figure 1. (**a**) Generalized geological map showing major tectonic structures due to the collision between India and Eurasia (revised from [49]); (**b**) Simplified geological map showing the distribution of Eocene–Oligocene (43–32 Ma) igneous rocks and fertile porphyry Cu–Mo–Au deposits in western Yunnan (modified from [32,35]); (**c**) Geologic map of the Tongchang–Chang'anchong porphyry deposit (modified from [50,51]).

3. Geology of Ore Deposits

The Tongchang–Chang'anchong porphyry deposit is geologically situated on the western margin of the South China (Yangtze) block. Many magmatic rocks are exposed in the area, including fine-grained syenites, pyroxene syenites, quartz syenite porphyries, syenite porphyries, diabases and diabase gabbros [52]. Exposed stratigraphy at Tongchang–Chang'anchong mainly includes Middle Silurian limestones and sandstones and Middle Ordovician sandstones.

The Tongchang–Chang'anchong porphyry deposit is composed of the Tongchang ore zone in the east and Chang'anchong ore zone in the west (Figure 1c). The Tongchang ore zone contains 8621 t Cu and 17,060 t Mo with 1.24% Cu and 0.218% Mo, whereas the Chang'anchong ore zone contains 29,337 t Cu and 13,310 t Mo with 1.48% Cu and 0.13% Mo [53]. The Tongchang–Chang'anchong porphyry deposit is hosted by Middle Silurian limestone and sandstone and spatially related to the quartz syenite porphyry intrusions (Figure 1c). The intrusions form stocks and dykes with outcrop areas of ~0.2 km^2 at the Tongchang ore zone and >0.18 km^2 at Chang'anchong ore zone, respectively [47].

The quartz syenite porphyries in both ore zones consist mainly of K-feldspar, plagioclase, quartz, amphibole and biotite. The main accessory minerals include titanite, zircon, and apatite (Figure 2). The ore zones have similar alteration mineral assemblages and mineralization styles [54]. From the inner quartz syenite porphyry to the outer wall-rock, three mineralization-related alteration zones are present. The inner alteration zone exhibits pervasive K-silicate and quartz–sericite alteration with disseminated molybdenite ± chalcopyrite and veinlets of molybdenite ± chalcopyrite mineralization. The skarn alteration zone at the contacts between the quartz syenite porphyry and the wall-rock is characterized by abundant skarn minerals (e.g., garnet, scapolite, tremolite, epidote and diopside), with massive Cu-sulfides and magnetite mineralization. The outer alteration zone in the wall-rocks is mainly composed of marble, with minor serpentine, quartz, chlorite, wollastonite and clinohumite [52].
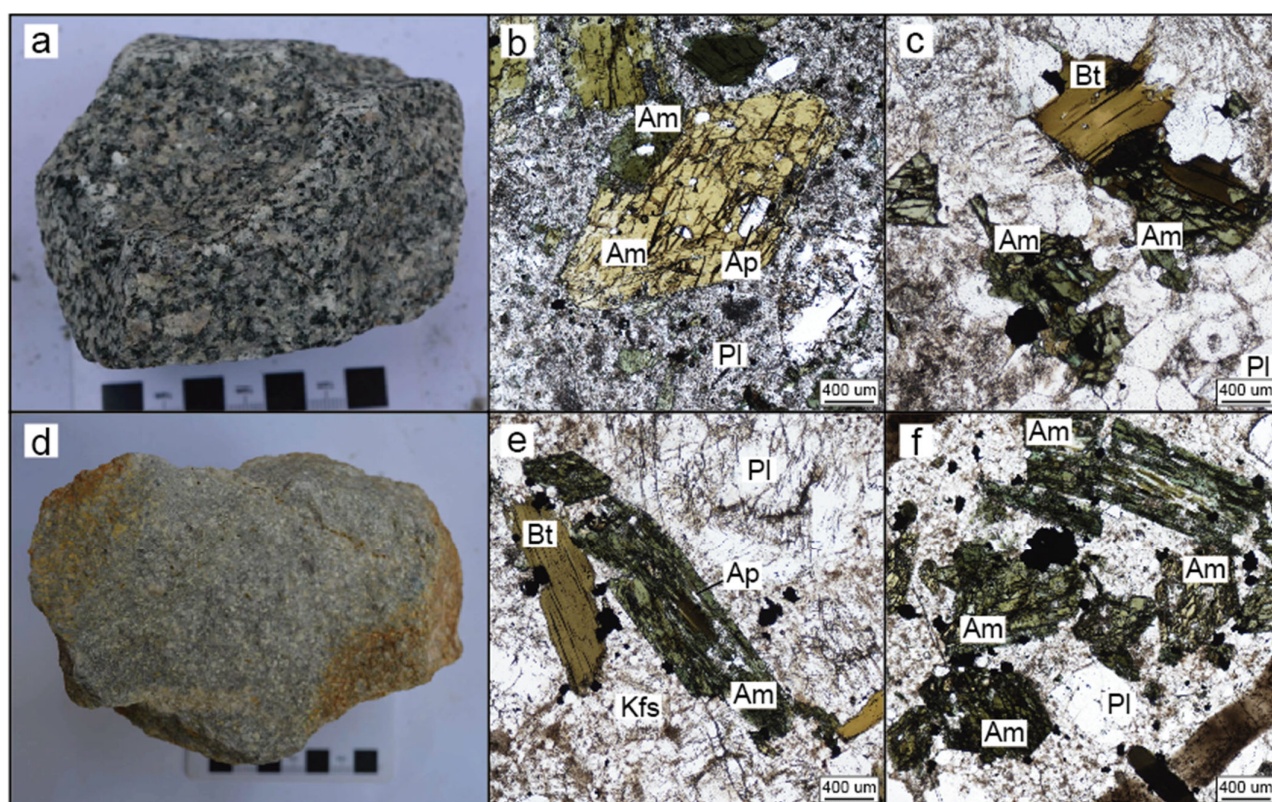
Figure 2. Photos of the quartz syenite porphyries from Tongchang–Chang'anchong porphyry deposit: (**a**) hand specimen of Tongchang quartz syenite porphyry; (**b**,**c**) photomicrographs of Tongchang quartz syenite porphyry; (**d**) hand specimen of Chang'anchong quartz syenite porphyry; (**e**,**f**) photomicrographs of Chang'anchong quartz syenite porphyry. Am, amphibole; Bt, biotite; Kfs, potassic feldspar; Pl, plagioclase; Ap, apatite.

4. Sampling and Analytical Methods

4.1. Sampling

Seven samples of unaltered quartz syenite porphyry were carefully selected from Tongchang and Chang'anchong for elemental analyses. The major element characteristics of amphibole, biotite and apatite in Tongchang and Chang'anchong fertile porphyries were studied using electron probe analysis (EMPA). Furthermore, trace element analyses of zircon and apatite in the fertile porphyries from Tongchang and Chang'anchong were carried out using laser ablation inductively coupled plasma mass spectrometry (LA–ICP–MS).

4.2. EMPA and LA–ICP–MS

4.2.1. Electron Microprobe Analysis

Amphibole, biotite and apatite were prepared as polished thin sections and studied in detail under a petrographic microscope (Figure 2). Major-element compositions of minerals were determined using an electron microprobe (JXA–8230) at the State Key Laboratory of Continental Dynamics, Northwest University, China. The instrument was operated at an accelerating voltage of 15 kV, beam current of 10 nA and beam diameter of 1 μm. Where possible, apatite crystals were analyzed with the c-axis parallel to the plane of the mount. This routine limits the potential for time dependent variability in halogen X-ray counts during analysis [55]. Microprobe standards of natural and synthetic phases were supplied by the SPI Company. The detection limit for major elements was 0.01 wt%, with an accuracy of ≤5%. Major element compositions are given in Supplementary Tables S1–S3.

4.2.2. LA–ICP–MS Trace Element Analysis

Zircon and apatite grains were identified by using a binocular microscope. They were pasted onto an epoxy target, and their center was polished (Figure 3).
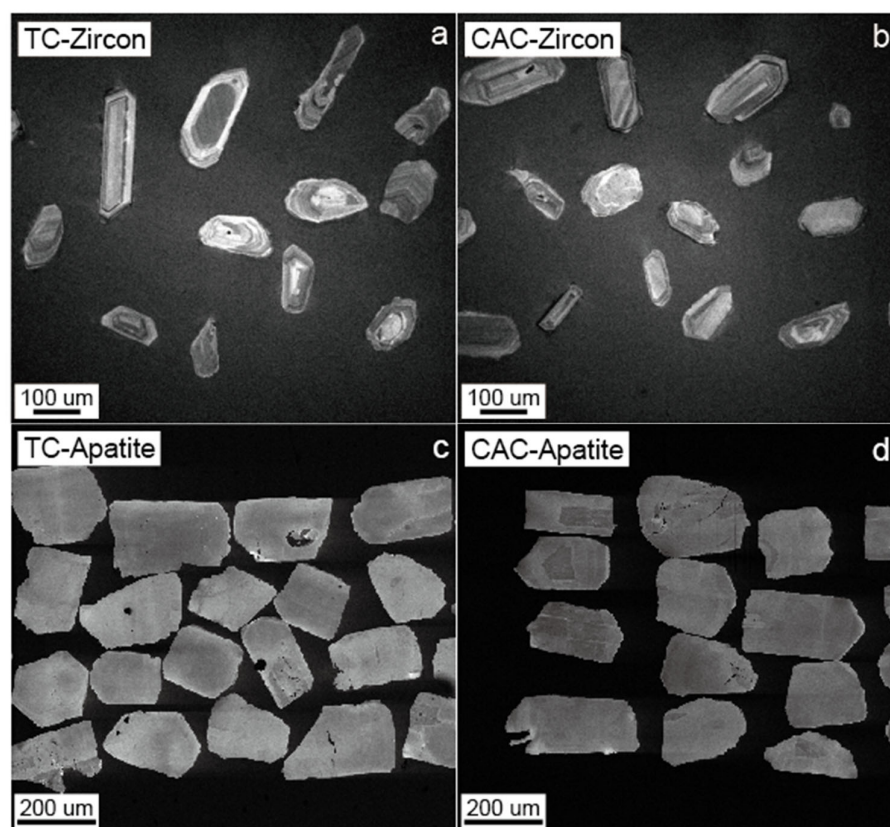
Figure 3. (**a**,**b**) Cathodoluminescence images of zircons from Tongchang and Chang'anchong quartz syenite porphyries. (**c**,**d**) Backscattered electron images of apatites from Tongchang and Chang'anchong quartz syenite porphyries.

Zircon trace element analyses were conducted at the Mineral Laser Microprobe Analysis Laboratory (Milma Lab), China University of Geosciences, Beijing, using the instruments of a quadrupole ICP–MS (Agilent 7900; Agilent Technologies, Santa Clara, CA, USA) and a NewWave 193UC Solid-State laser ablation system (193 nm; Elemental Scientific Lasers, Bozeman, MT, USA) with an automatic positioning system. A laser spot size of 35 μm, laser energy density of 6 J/cm^2 and a repetition rate of 8 Hz were used for analysis. The ablated sample material was carried into the ICP–MS system by high-purity helium gas. Calibrations for the zircon analyses were carried out using the NIST 610 glass as external

standards and Si as the internal standard. Trace element concentrations of zircons were calculated using ICPMSDataCal (ver. 10.1) [56,57]. Analytical results are given in Table S4.

Trace elements analysis of apatite were performed at the in situ Mineral Geochemistry Lab, Ore Deposit and Exploration Centre (ODEC), Hefei University of Technology, China, with Laser Ablation Inductively-Coupled Plasma Mass Spectrometry (LA–ICP–MS) (beam size diameter: 70 µm; energy density: 2.5 J/cm^2; laser pulse frequency: 7 Hz). The trace element concentrations of apatite were calculated with standard SRM 610 as the external calibration. The ICPMSDataCal software (ver. 10.1) was adopted to perform off-line correction by using Ca as an internal standard element [56,57]. Analytical results are given in Table S5.

## 5. Results: Mineral Compositions and Crystallization Conditions

5.1. Biotite

Biotites from Tongchang and Chang'anchong quartz syenite porphyries have similar compositions, with FeO^T and MgO contents ranging from 16.06 to 18.33 wt% and 12.73 to 15.79 wt%, respectively. All of these biotites, with low Mg/(Mg + Fe) from 0.56 to 0.64, plot in the field of biotite, according to the classification scheme of [58] (Figure 4a).

The calculated temperatures of Tongchang–Chang'anchong biotites display the range of 776–830 °C, using the thermometer of [59]. We also calculated the Cl/OH ratios in the melt by the compositions of biotites according to the method of [60]. The melt Cl/OH ratios calculated by biotites are 0.013–0.033 (Table S1).

5.2. Amphibole

The amphibole composition data for the Tongchang–Chang'anchong quartz syenite porphyries are compiled in Table S2. Amphibole formulae were calculated on the basis of a 13-cation normalization following the guidelines of [61]. According to the classification of [62], all amphiboles from Tongchang–Chang'anchong quartz syenite porphyries are magnesio-hornblende (Figure 4b). The amphibole Cl contents are scattered and vary from 0.02–0.30 wt%. The amphiboles from Tongchang and Chang'anchong cannot be distinguished by their compositional characteristics. The calculated melt Cl/OH ratios, using the amphibole compositions, range from 0.002–0.038 according to the method of [63] (Table S2).
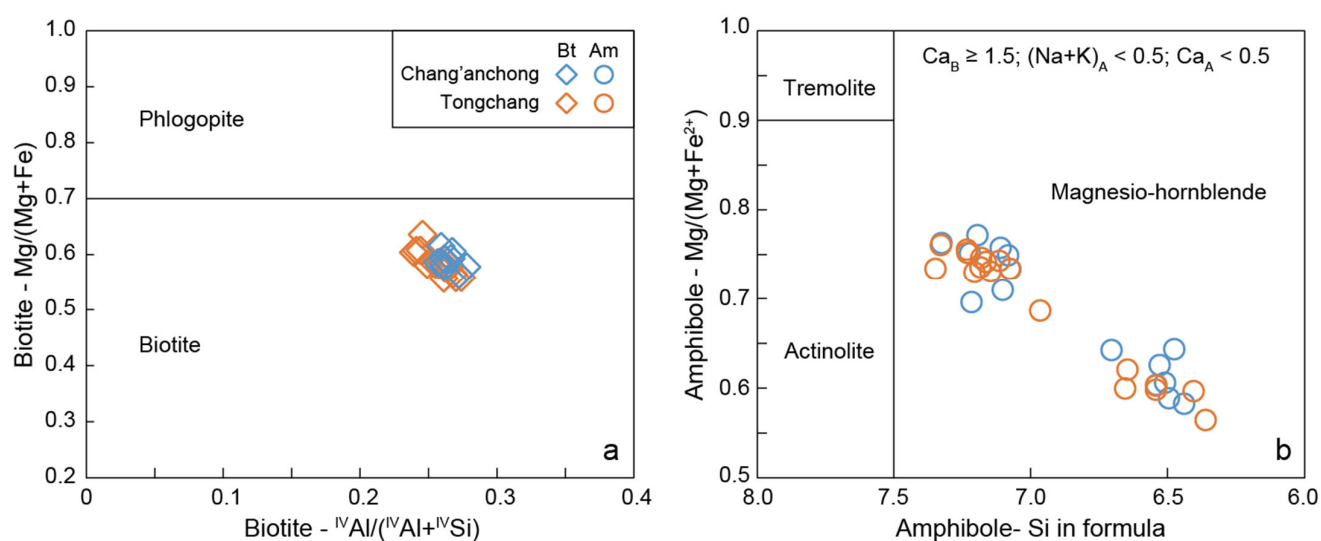
Figure 4. Illustrations of biotite and amphibole compositions from Tongchang and Chang'anchong quartz syenite porphyries. (**a**) Plots in Mg/(Mg + Fe) vs. ^{IV}Al/(^{IV}Al + ^{IV}Si) binary diagram for biotite (after [58]); (**b**) Plots in Si in formula vs. Mg/(Mg + Fe^{2+}) binary diagram for amphibole (after [62]).

Amphibole is stable across a wide P–T range (e.g., 600–1100 °C and 0.1–25 kbar) in hydrous magmas [64–66]. It is often used to rebuild the thermodynamic structure of its host magma during fractional crystallization, e.g., [14,23,67–70]. Intensive parameters (P, T, $f\mathrm{O_2}$, $\mathrm{H_2O}$ in melt) at the time of amphibole crystallization were estimated based on amphibole compositions using the empirical formulations of [69], despite debates on the accuracy of the calculated parameters using these empirical calibrations, e.g., [71,72]. Chelle-Michou et al. [18] used independent mineralogical, chemical and thermodynamic constraints to argue that they represent overall reasonable estimates of intensive parameters for the magmas in equilibrium with amphiboles. Meanwhile, Gorini et al. [73] found that the crystallization depths calculated by the amphiboles are thus consistent with the seismic tomography model for the same magma body, pointing out a good precision and reliability of the method from [69]. The calculated temperatures, pressures, $f\mathrm{O_2}$ (ΔFMQ) and $\mathrm{H_2O}$ in melt contents for crystallization of the amphiboles are 688–833 °C, 0.52–2.23 kbar, +2.06 to +3.86 and 2.67–4.34 wt%, respectively. The results are listed in Table S2.
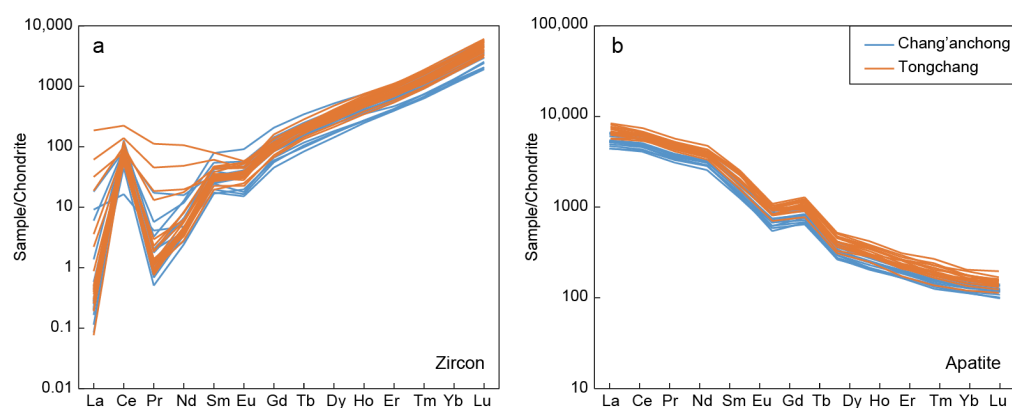
5.3. Zircon

Zircons from Tongchang–Chang'anchong quartz syenite porphyries display heavy REEs (HREE) enrichment relative to light REEs (LREE), with positive Ce and slightly negative Eu anomalies (Figure 5a). The zircons have low Th/U ratios (0.36–1.00). The Yb/Gd and Ce/Sm ratios are 10.08–23.86 and 3.75–11.28, respectively (Table S4). Their euhedral oscillatory zoning in cathodoluminescence images (Figure 3a,b) and the characteristics of their REE patterns (Figure 5a) suggest that they are magmatic zircons [20,74,75].

The crystallization temperatures for Tongchang–Chang'anchong zircons, calculated using the thermometer of [74], range from 651 to 815 °C. The methods of [20] are used to quantify the $f\mathrm{O_2}$ values for these zircons, ranging with wide ΔFMQ values of +0.25 to +2.92. The results are reported in Table S4.

5.4. Apatite

The compositions of apatites from Tongchang–Chang'anchong quartz syenite porphyries are listed in Tables S3 and S5. Apatites in Tongchang and Chang'anchong quartz syenite porphyries exhibit similar CaO and $\mathrm{P_2O_5}$ contents (53.5–55.5 wt% and 40.7–42.6 wt%). The Cl and F contents of them are 0.10–0.38 wt% and 2.10–2.62 wt%, respectively. The mole fractions of F, Cl and OH (X_F, X_{Cl} and X_{OH}) were calculated by the Cl and F contents of these apatites [55,76]. The X_{Cl}/X_{OH}, X_F/X_{OH} and X_F/X_{Cl} ratios of Tongchang–Chang'anchong apatites are 0.04–0.22, 1.54–2.93 and 10.35–48.24, respectively (Table S3). Contents of all other major elements of the apatites are low. The Tongchang–Chang'anchong apatites show high Sr/Y ratios (1.21–4.15), low Y contents (353–639 ppm), weakly negative Eu anomaly and pronounced HREE depletion (Figure 5b).

Figure 5. Chondrite-normalized REE patterns of (**a**) zircon and (**b**) apatite of Tongchang and Chang'anchong quartz syenite porphyries. Chondrite values are after [77].

6. Discussion

6.1. The Magmatic Source and Crystallization Sequence

6.1.1. Discriminant for Adakite from Apatite Geochemistry

Adakite is geochemically characterized by high Al_2O_3 and Sr contents, low Y and HREE contents, lack of Eu anomaly and as coupled with high Sr/Y and $(La/Yb)_N$ ratios [78]. The models of petrogenesis of adakite have progressively expanded compared with the initial naming of "adakite" related to a specific tectonic setting. From the perspective of magma evolution, the residue of garnet and amphibole and the decomposition of plagioclase in the magma source play a vital role in producing the high Sr content, less pronounced to absent Eu anomaly and the lower HREE content assigned to adakites [79].

Previous studies focused on geochemical features of apatite crystallizing from adakitic and nonadakitic plutons revealed that the Sr, Y, Eu/Eu* and REE contents in apatites can be indicative of adakitic affinities, e.g., [80–82]. This is fairly useful for distinguishing the adakitic-like features of highly altered or weathered rocks as long as early-crystallized apatite grains were preserved. In this study, apatite grains from Tongchang and Chang'anchong fertile intrusions are all plotted within the adakite-like fields in the ternary discrimination diagram of 1000/(Eu/Eu*)–10*Sr–HREY and the bioplot of Sr vs. HREY (Gd ~ Lu + Y) of apatites (Figure 6a,b), indicating that these apatite-bearing fertile porphyries possess adakitic characteristics. This result is consistent with the whole-rock geochemical data of the Tongchang–Chang'anchong fertile porphyries [47,52–54,83].
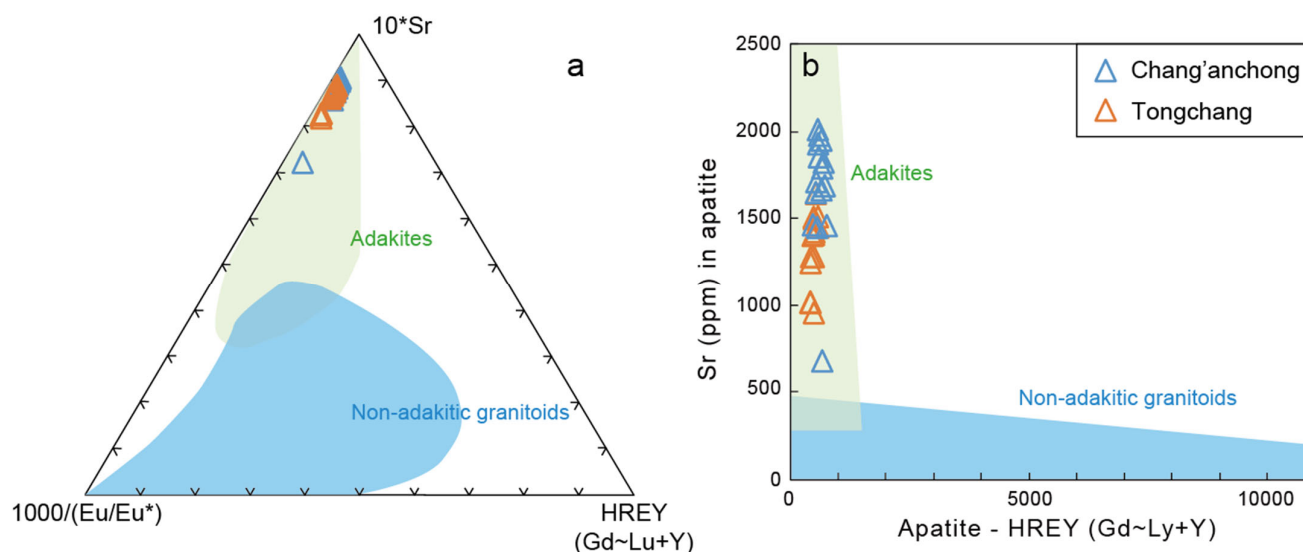

Figure 6. (**a**) Ternarydiscriminationdiagram of 1000/(Eu/Eu*)–10*Sr–HREY for apatite; (**b**) biplot of Sr vs. HREY of apatites, which shows two unique fields for adakites and nonadakitic granitoids [82].

According to the previous studies, the chemical compositions of the Tongchang–Chang'anchong fertile porphyries have high SiO_2 and low MgO contents, typical of igneous rocks formed from crust-derived melts. Based on the similar Sr–Nd isotope compositions of these rocks with the mafic lower crust beneath the Yangtze Craton ($^{87}Sr/^{86}Sr$ = 0.7060–0.7100; $\varepsilon_{Nd}(t)$ = −10.0 to 0) [84] and the adakitic characteristics according to the geochemical data of whole-rock and apatite, the magmatic source of Tongchang–Chang'anchong fertile intrusions is restricted to the mafic lower crust. The zircons from these fertile intrusions have Neoproterozoic Hf isotope model age, indicating that the Tongchang–Chang'anchong fertile intrusions were derived from partial melting of the Neoproterozoic juvenile lower crust [52,83].

6.1.2. The Crystallization Sequence of Tongchang–Chang'anchong Fertile Porphyries

Systematically decreasing Ti-in-zircon concentrations (2.48–15.14 ppm) recorded in Tongchang–Chang'anchong fertile intrusions indicate zircon crystallization from progressively cooler melts in a larger magma source region (Table S4) [74]. The temperature decrease is correlated with decreasing Th/U and increasing Yb/Gd and Ce/Sm that are typically driven by cocrystallization of other accessory minerals [85–87]. The increases in Ce/Sm and Yb/Gd resulted from preferential removal of MREE (Sm, Gd) from the melt compared to LREE and HREE, producing the decreased convexity of the REE pattern characteristic of the Tongchang–Chang'anchong fertile intrusions (Figures 5a and 7a). The diversity of zircon compositions along the observed evolutionary paths apparently reflects different proportions of amphibole, apatite and titanite crystallization. The vectors in Figure 7a illustrate the effect of crystallization of amphibole, apatite, titanite and zircon by available mineral–melt partition coefficients for basalt and andesite [86]. The linear array of Tongchang–Chang'anchong fertile intrusions in Ce/Sm versus Yb/Gd plots has a shallow slope, indicating the dominated crystallization of amphibole during the crystallization of zircons (Figure 7a).
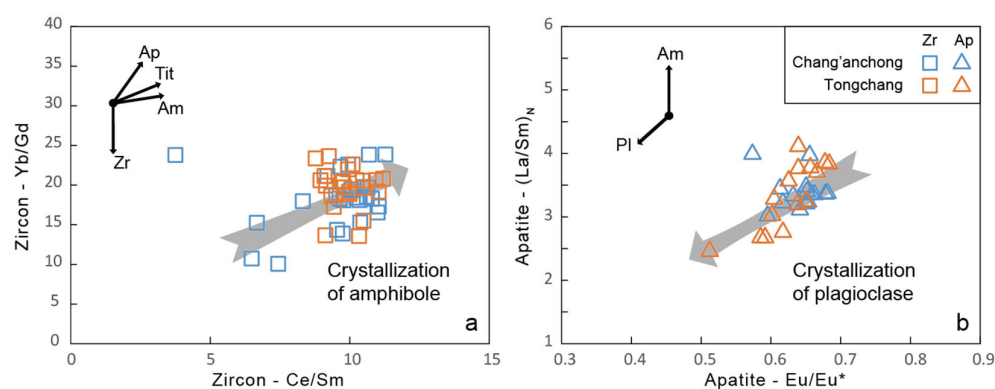
Figure 7. (**a**) Plots of zircon Ce/Sm vs. Yb/Gd; and (**b**) apatite Eu/Eu* vs. (La/Sm)$_N$. The continuous-line arrows represent fractional crystallization vectors [83,87]. Ap, apatite; Tit, titanate; Am, amphibole; Pl, plagioclase; Zr, zircon.

The early crystallization of plagioclase plays a significant role in the Eu/Eu* content of the melt during magma evolution. Both zircon and apatite have relatively obvious negative Eu anomalies, indicating that plagioclase crystallization differentiation occurred at a very early stage (Figure 5). The MREE enrichment in apatite is mainly controlled by their high partition coefficients, but apatite crystallized from a residual melt dominated by amphibole fractionation would result in MREE depletion and the increase (La/Sm)$_N$. Thus, apatites show no MREE depletion (Figure 5b) with low (La/Sm)$_N$ ratios, and the decreasing (La/Sm)$_N$ corresponds with a similar decreasing trend of Eu/Eu* in apatites, revealing the dominated crystallization of plagioclase instead of amphibole (Figure 7b) [82].

Combined with the thermometer calculation results of zircon, amphibole and biotite, and the textural relationships, the crystallization sequence of the Tongchang–Chang'anchong fertile intrusions could be established. The plagioclase first began to crystallize, then apatite began to crystallize following the crystallization process of plagioclase. The amphibole and biotite began to crystallize later, and finally zircon began to crystallize.

6.2. The magma H$_2$O Contents and fO$_2$ Conditions during Upper Crustal Evolution

According to the results of amphibole thermobarometer and biotite and zircon thermometers, the minerals mainly record the magmatic evolution process of the Tongchang–Chang'anchong fertile porphyries above 10 km depth. Together with the chemical composition of minerals and the sequence of crystallization, we can define the physical and chemical magmatic evolution process of the Tongchang–Chang'anchong fertile porphyries in the upper crust.

The fluctuation of magma H_2O and fO_2 during upper crustal (< 10 km depth) evolution is illustrated in Figures 8 and 9a. The amphibole with the highest crystallization temperatures (~850 °C) reveal that the primary magma had high initial fO_2 (ΔFMQ) values of $\geq +3.0$ and relatively high H_2O content of ≥ 3.5 wt% (Figure 8b,c and Figure 9a). Upon the cooling process of the magma evolution from ~850 to ~790 °C, the magmatic H_2O content slightly increased from ~3.5 to ~4.4 wt%, as indicated by the positive correlation between crystallization temperatures and H_2O contents for amphiboles (Figure 8c). Such an increase resulted from the magma evolution under an H_2O-unsaturated condition. The H_2O content of the magma will gradually increase with the magmatic evolution until it becomes H_2O-saturated and the magmatic fluid begins to dissolve from the melt, according to H_2O solubility in melts (Figure 8b) [21,22,88,89]. The fO_2 (ΔFMQ) decreased from $\geq +3.0$ to ~+2.0 during this process. Considering the reduced nature of the limestone formation, it is proposed that the decrease in fO_2 was caused by contamination with this formation, during which reduced materials such as organic carbon were added to the melt, buffering its fO_2.
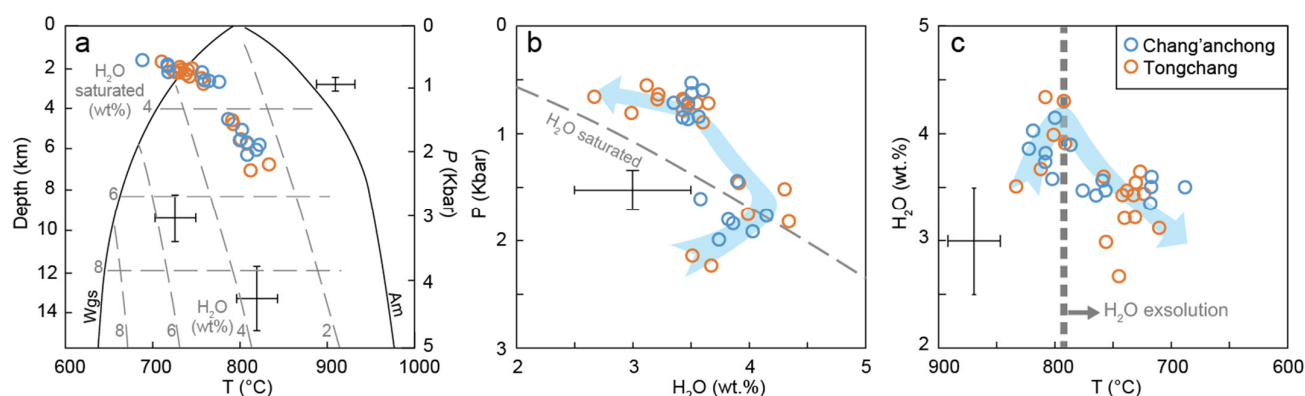
Figure 8. (**a**) The calculated P–T conditions for Tongchang and Chang'anchong quartz syenite porphyries. Cross bars indicate the P–T uncertainties [69]. Liquidus for amphibole is delineated with black solid lines, labeled on their unstable side [90]. The wet granite solidus (Wgs) line is delineated with a black solid line [89]. The steep grey dashed lines are undersaturated liquidus (with wt% H_2O labeled) and the subhorizontal dashed lines are H_2O solubility limits (also labeled as H_2O saturated) [88,89]. Am, amphibole; Wgs, wet granite solidus. (**b**) The calculated pressure condition vs. magmatic H_2O content for Tongchang and Chang'anchong quartz syenite porphyries. Cross bars indicate the P–H_2O uncertainties [69]. The dashed line shows the H_2O solubility curves [88]. (**c**) The calculated T–H_2O conditions for Tongchang and Chang'anchong quartz syenite porphyries. Cross bars indicate the T–H_2O uncertainties [69]. The thick dashed line represents the H_2O exsolution process.

Subsequently, the temperature of the melt continued to drop from ~790 °C, and the H_2O content of the melt decreased from ~4.4 wt% constantly. This suggests that the magma reached H_2O saturation and triggered H_2O exsolution during this process, as the H_2O solubility of the melt decreased with the ascent and fractionation of the magma (Figure 8a,b). However, the fO_2 (ΔFMQ) increased from ~+2.0 to ~+3.4 first during the temperature of ~790–~750 °C, and then decreased from ~+3.4 to ~+0.6. The fO_2 increase was probably caused by the H_2O exsolution discussed above. Wall-rock contamination may have been ongoing during H_2O exsolution at the temperature of ~790–~750 °C, but the impact of H_2O exsolution on the melt probably surpassed that of contamination. Previous studies have found that H_2O exsolution at shallow depths (< 4 km) may oxidize magma and increase fO_2 by about 1–2 log units, e.g., [23,91]. This is because (1) H_2O exsolution of reduced and/or weakly oxidized species of C, H and S would directly increase magmatic fO_2 [5,92–97], and (2) exsolution of chlorine-rich aqueous volatiles would increase magmatic fO_2 by self-oxidation (increasing Fe^{3+}/Fe^{2+} ratios in residual melt) due to preferential extraction of Fe^{2+} into the chlorine-rich volatile phase [98]. As the melt continued to evolve

and the temperature was less than ~750 °C, wall-rock contamination took the leading role and made the fO_2 (ΔFMQ) of the magma decrease from ~+3.4 to ~+0.6.
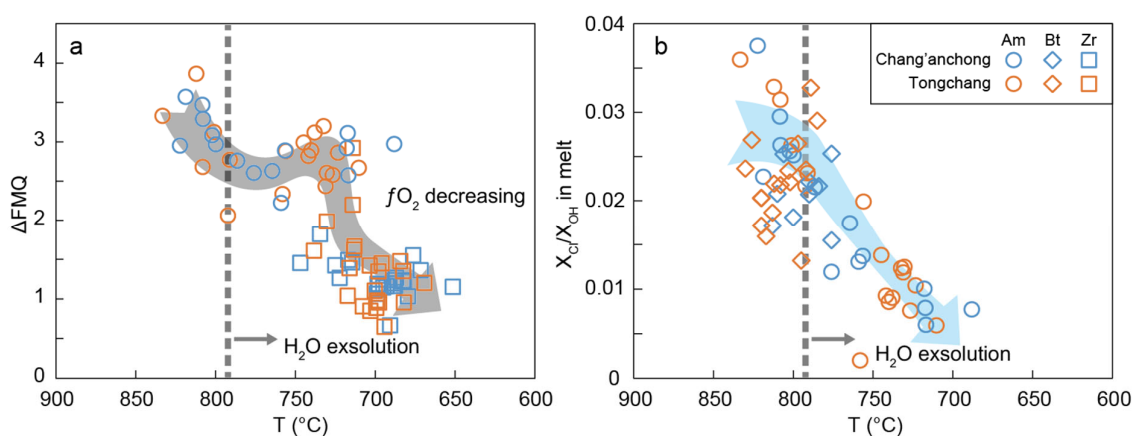
Figure 9. The calculated (**a**) fO_2 (ΔFMQ) vs. T and (**b**) X_{Cl}/X_{OH} in melt vs. T conditions for Tongchang and Chang'anchong quartz syenite porphyries. The thick dashed line represents the H_2O exsolution process. Am, amphibole; Bt, biotite; Zr, zircon.

*6.3. Fluid Exsolution and Implications for the Formation of PCDs*

Early saturation of magmatic fluid in porphyry magma is generally considered a prerequisite for the formation of PCDs, with exsolution of the fluid phase maximizing contents of crystal- or sulfide-compatible ore metals (e.g., Cu and Au) still dissolved in the melt, e.g., [13,99]. However, the timing of magmatic fluid saturation in PCDs is not well constrained.

Apatite crystals incorporate Cl and F as essential structural constituents, thus preserving sensitive records of halogen evolution in magmatic systems [93]. Therefore, we built on the model of [76] to estimate the composition of apatite crystallizing in equilibrium with melt and to verify the fluid exsolution process. The starting melt composition was assumed as 850 ppm Cl, 1600 ppm F and 3.5 wt% H_2O, according to the features of apatite and the results calculated by amphibole. The model results are in good agreement with the compositional characteristics of apatites, as shown in Figure 10. The model suggests that the initial magma underwent 22% fractional crystallization under H_2O-unsaturated condition. Apatite compositions typically show a decrease in X_{Cl}/X_{OH}, X_F/X_{OH} and X_F/X_{Cl} ratios. The H_2O content in the melt continued to increase, eventually reaching 4.5 wt% and becoming H_2O saturated during this process. Subsequently, the magma continued to 70% crystallization under conditions of H_2O-saturation, which is characterized by a strong decrease in apatite X_{Cl}/X_{OH} ratio with increasing X_F/X_{Cl} and an initial decrease followed by an increase in X_F/X_{OH} (Figure 10). This process was accompanied by the continuous exsolution of magmatic fluid.

Based on the model according to apatite, we used multiple minerals to further define the magma evolution process and the accompanying fluid exsolution process and fO_2 changes, as well as the relationship between these processes and the mineralization of PCDs.

The very early H_2O content in the melt calculated by amphibole was ~3.5 wt%, which is lower than its H_2O-solubility (Figure 8b). During the process of magma evolution under the H_2O-unsaturated condition, the H_2O content in the melt continually increased (Figure 8c). Meanwhile, the Cl/OH ratio in the melt should slightly decrease or remain relatively stable, based on the experimental exchange partition coefficient of Cl/OH and Cl/H_2O ratios between fluid and melt [63,100]. The Cl/OH ratios in the melt, calculated using amphibole and biotite, show a relatively flat trend prior to 790 °C, indicating no obvious fluid exsolution. As the magma continued to evolve, the temperature decreased to below 790 °C and the H_2O content in the melt began to decline. At the same time, the Cl/OH ratio in the melt also underwent a significant and sustained decrease, indicating that fluid saturation occurred near 790 °C. During the early stage of fluid exsolution

(790–750 °C), the magma maintained a relatively high fO_2 (ΔFMQ > +2), preventing sulfide saturation in the melt. As a result, there were high contents of metals dissolved in the melt. The high fO_2 also led to low $D^{fluid/melt}$ S partitioning [101], and exsolved fluid would therefore be characterized by high SO_2/H_2S ratios. Cl is also incompatible in the melt and is partitioned strongly into an exsolved fluid phase, which can form complexes and effectively aggregate ore metals [100,102]. The high SO_2/H_2S and Cl in the exsolved magmatic fluid enabled a large number of ore-forming metals to be distributed in the fluid during the process of fluid exsolution from the melt, forming ore-forming fluids. When the temperature was below 750 °C, the decreasing fO_2 of the melt caused sulfide saturation, and the ability of the exsolved fluid to transport metals was weakened, thereby restricting the further upward migration of the ore-forming components. This may be one of the key factors limiting the Tongchang–Chang'anchong fertile intrusions to form a giant PCD.
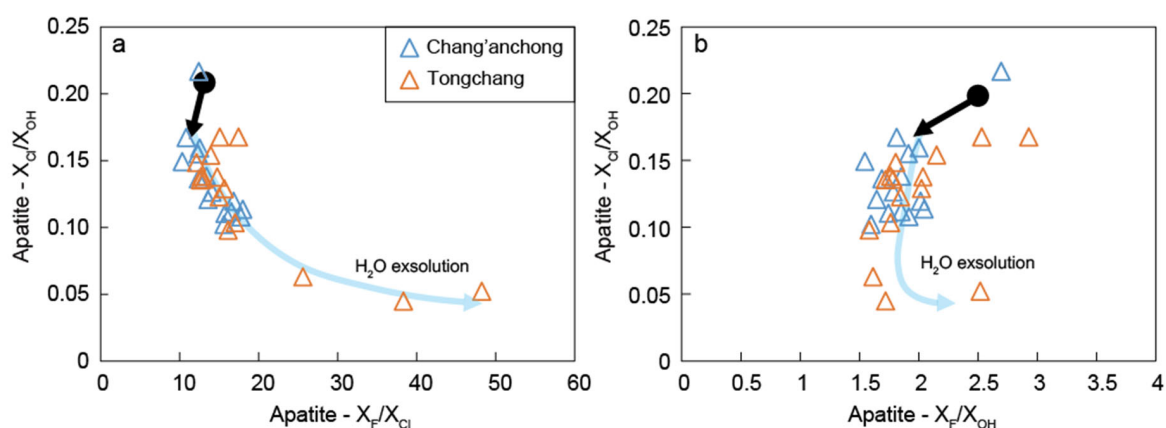
Figure 10. Volatile compositions of apatites from Tongchang and Chang'anchong quartz syenite porphyries. (**a**) Apatite volatile compositions in X_{Cl}/X_{OH} vs. X_F/X_{Cl} and (**b**) X_{Cl}/X_{OH} vs. X_F/X_{OH}. Apatite crystallization begins at the black point and continues to 22% crystallization under H_2O-undersaturated condition according to the black arrow (initial H_2O content is 3.5%; $D^{c/m}$ F $\approx$ 1.3 and $D^{c/m}$ Cl $\approx$ 1). Then, apatite compositional evolution continues in the blue arrow to 70% crystallization under H_2O-saturated condition.

7. Conclusions

Based on mineralogical analyses and calculations, the magma of the fertile porphyries (quartz syenite porphyries) in the Tongchang–Chang'anchong porphyry deposit display a high initial fO_2, with ΔFMQ $\geq$ +3.0. This initially highly oxidized magma underwent magmatic processes such as magma evolution, contamination, as well as H_2O exsolution within upper crust, causing the fluctuation of magmatic fO_2.

The findings suggest that the fluid exsolution process of the Tongchang–Chang'anchong porphyry deposit occurred at ~790 °C, which was the early stage of the magma evolution process. The magma's high fO_2 allowed for efficient extraction of a large amount of ore-forming minerals to the magmatic fluid, representing the ore-forming fluid. This ore-forming would eventually move upward and form porphyritic mineralization. Subsequently, due to the relatively reduced wall-rock contamination, fO_2 of the magma continued to decrease, leading to the formation of sulfides containing ore-forming metals (such as Cu and Au), which could no longer be transported by the exsolved magmatic fluid. This continuous fO_2 decrease during the fluid exsolution process may be a crucial factor preventing the formation of a giant PCD in Tongchang–Chang'anchong.

References

1. Sillitoe, R.H. Porphyry Copper Systems. *Econ. Geol.* **2010**, *105*, 3–41. [CrossRef]
2. Wilkinson, J.J. Triggers for the formation of porphyry ore deposits in magmatic arcs. *Nat. Geosci.* **2013**, *6*, 917–925. [CrossRef]
3. Richards, J.P. A Shake-Up in the Porphyry World? *Econ. Geol.* **2018**, *113*, 1225–1233. [CrossRef]
4. Richards, J.P.; Spell, T.; Rameh, E.; Razique, A.; Fletcher, T. High Sr/Y magmas reflect arc maturity, high magmatic water content, and porphyry Cu±Mo±Au potential: Examples from the Tethyan arcs of central and eastern Iran and western Pakistan. *Econ. Geol.* **2012**, *107*, 295–332. [CrossRef]
5. Richards, J.P. The oxidation state, and sulfur and Cu contents of arc magmas: Implications for metallogeny. *Lithos* **2015**, *233*, 27–45. [CrossRef]
6. Loucks, R. Distinctive composition of copper-ore-forming arcmagmas. *Aust. J. Earth Sci.* **2014**, *61*, 5–16. [CrossRef]
7. Loucks, R.R. Deep entrapment of buoyant magmas by orogenic tectonic stress: Its role in producing continental crust, adakites, and porphyry copper deposits. *Earth-Sci. Rev.* **2021**, *220*, 103744. [CrossRef]
8. Chiaradia, M. Crustal thickness control on Sr/Y signatures of recent arc magmas: An Earth scale perspective. *Sci. Rep.* **2015**, *5*, 8115. [CrossRef]
9. Mungall, J.E. Roasting the mantle: Slab melting and the genesis of major Au and Au-rich Cu deposits. *Geology* **2002**, *30*, 915–918. [CrossRef]
10. Burnham, C.W. *Magmas and Hydrothermal Fluids: Geochemistry of Hydrothermal Ore Deposits*; Wiley: New York, NY, USA, 1979; pp. 71–136.
11. Hedenquist, J.W.; Lowenstern, J.B. The role of magmas in the formation of hydrothermal ore deposits. *Nature* **1994**, *370*, 519–527. [CrossRef]
12. Audétat, A.; Simon, A.C. *Magmatic Controls on Porphyry Copper Genesis*; Society of Economic Geologists: McLean, VA, USA, 2012.
13. Candela, P.A. A review of shallow, ore-related granites: Textures, volatiles, and ore metals. *J. Petrol.* **1997**, *38*, 1619–1633. [CrossRef]
14. Ridolfi, F.; Renzulli, A.; Puerini, M. Stability and chemical equilibrium of amphibole in calc-alkaline magmas: An overview, new thermobarometric formulations and application to subduction-related volcanoes. *Contrib. Miner. Pet.* **2010**, *160*, 45–66. [CrossRef]
15. Tiepolo, M.; Tribuzio, R.; Langone, A. High-Mg Andesite Petrogenesis by Amphibole Crystallization and Ultramafic Crust Assimilation: Evidence from Adamello Hornblendites (Central Alps, Italy). *J. Pet.* **2011**, *52*, 1011–1045. [CrossRef]
16. Krawczynski, M.J.; Grove, T.L.; Behrens, H. Amphibole stability in primitive arc magmas: Effects of temperature, H_2O content, and oxygen fugacity. *Contrib. Miner. Pet.* **2012**, *164*, 317–339. [CrossRef]
17. Nandedkar, R.H.; Hürlimann, N.; Ulmer, P.; Müntener, O. Amphibole–melt trace element partitioning of fractionating calc-alkaline magmas in the lower crust: An experimental study. *Contrib. Miner. Pet.* **2016**, *171*, 71. [CrossRef]
18. Chelle-Michou, C.; Chiaradia, M.; Béguelin, P.; Ulianov, A. Petrological evolution of the magmatic suite associated with the Coroccohuayco Cu (–Au–Fe) Porphyry–skarn deposit, Peru. *J. Petrol.* **2015**, *56*, 1829–1862. [CrossRef]

19. Chelle-Michou, C.; Chiaradia, M. Amphibole and apatite insights into the evolution and mass balance of Cl and S in magmas associated with porphyry copper deposits. *Contrib. Miner. Pet.* **2017**, *172*, 105. [CrossRef]

20. Loucks, R.R.; Fiorentini, M.L.; Henríquez, G.J. New Magmatic Oxybarometer Using Trace Elements in Zircon. *J. Pet.* **2020**, *61*, egaa034. [CrossRef]

21. Khedr, M.Z.; Takazawa, E.; Arai, S.; Stern, R.J.; Morishita, T.; El-Awady, A. Styles of Fe–Ti–V ore deposits in the Neoproterozoic layered mafic-ultramafic intrusions, south Eastern Desert of Egypt: Evidence for fractional crystallization of V-rich melts. *J. Afr. Earth Sci.* **2022**, *194*, 104620. [CrossRef]

22. Khedr, M.Z.; El-Awady, A.; Arai, S.; Hauzenberger, C.; Tamura, A.; Stern, R.J.; Morishita, T. Petrogenesis of the ~740 Korab Kansi mafic–ultramafic intrusion, South Eastern Desert of Egypt: Evidence of Ti-rich ferropicritic magmatism. *Gondwana Res.* **2020**, *82*, 48–72. [CrossRef]

23. Li, W.K.; Yang, Z.M.; Cao, K.; Lu, Y.; Sun, M. Redox-controlled generation of the giant porphyry Cu–Au deposit at Pulang, southwest China. *Contrib. Mineral. Petrol.* **2019**, *174*, 1–34. [CrossRef]

24. Large, S.J.E.; Buret, Y.; Jörn-Frederik Wotzlaw, J.F.; Karakas, O.; Guillong, M.; von Quadt, A.; Heinrich, C.A. Copper-mineralised porphyries sample the evolution of a large-volume silicic magma reservoir from rapid assembly to solidification. *Earth Planet. Sci. Lett.* **2021**, *563*, 116877. [CrossRef]

25. Zhang, C.; Holtz, F.; Ma, C.; Wolff, P.E.; Li, X. Tracing the evolution and distribution of F and Cl in plutonic systems from volatile-bearing minerals: A case study from the Liujiawa pluton (Dabie orogen, China). *Contrib. Miner. Pet.* **2012**, *164*, 859–879. [CrossRef]

26. Cocks, L.R.M.; Torsvik, T.H. The dynamic evolution of the Palaeozoic geography of eastern Asia. *Earth-Sci. Rev.* **2013**, *117*, 40–79. [CrossRef]

27. Chung, S.L.; Lo, C.H.; Lee, T.Y.; Zhang, Y.; Xie, Y.; Li, X.; Wang, K.L.; Wang, P.L. Diachronous uplift of the Tibetan plateau starting 40?Myr ago. *Nature* **1998**, *394*, 769–773. [CrossRef]

28. Chung, S.L.; Chu, M.F.; Zhang, Y.; Xie, Y.; Lo, C.H.; Lee, T.Y.; Lan, C.Y.; Li, X.; Zhang, Q.; Wang, Y. Tibetan tectonic evolution inferred from spatial and temporal variations in post-collisional magmatism. *Earth-Sci. Rev.* **2005**, *68*, 173–196. [CrossRef]

29. Wang, J.H.; Yin, A.; Harrison, T.; Grove, M.; Zhang, Y.Q.; Xie, G.H. A tectonic model for Cenozoic igneous activities in the eastern Indo–Asian collision zone. *Earth Planet. Sci. Lett.* **2001**, *188*, 123–133. [CrossRef]

30. Lu, Y.J.; Kerrich, R.; Peter Cawood, P.; McCuaig, T.C.; Hart, C.J.R.; Li, Z.X.; Hou, Z.; Bagas, L. Zircon SHRIMP U–Pb geochronology of potassic felsic intrusions in western Yunnan, SW China: Constraints on the relationship of magmatism to the Jinsha suture. *Gondwana Res.* **2012**, *22*, 737–747. [CrossRef]

31. Campbell, I.H.; Stepanov, A.S.; Liang, H.Y.; Allen, C.M.; Norman, M.; Zhang, Y.Q.; Xie, Y.W. The origin of shoshonites: New insights from the Tertiary high-potassium intrusions of eastern Tibet. *Contrib. Miner. Pet.* **2014**, *167*, 983–1004. [CrossRef]

32. Deng, J.; Wang, Q.F.; Li, G.; Santosh, M. Cenozoic tectono–magmatic and metallogenic processes in the Sanjiang region, southwestern China. *Earth-Sci. Rev.* **2014**, *138*, 268–299. [CrossRef]

33. Hou, Z.Q.; Ma, H.W.; Khin, Z.; Zhang, Y.; Wang, M.; Wang, Z.; Pan, G.; Tang, R. The Himalayan Yulong porphyry copper belt: Product of large-scale strike-slip faulting in eastern Tibet. *Econ. Geol.* **2003**, *98*, 125–145.

34. Hou, Z.Q.; Zhou, Y.; Wang, R.; Zheng, Y.C.; He, W.Y.; Zhao, M.; Evans, N.; Weinberg, R.F. Recycling of metal-fertilized lower continental crust: Origin of non-arc Au-rich porphyry deposits at cratonic edges. *Geology* **2017**, *45*, 563–566. [CrossRef]

35. Lu, Y.J.; Kerrich, R.; Kemp, A.I.; McCuaig, T.C.; Hou, Z.Q.; Hart, C.J.; Li, Z.X.; Cawood, P.A.; Bagas, L.; Yang, Z.M.; et al. Intracontinental Eocene–Oligocene porphyry Cu mineral systems of Yunnan, Western Yangtze Craton, China: Compositional characteristics, sources, and implications for continental collision metallogeny. *Econ. Geol.* **2013**, *108*, 1541–1576. [CrossRef]

36. He, W.Y.; Mo, X.X.; He, Z.H.; White, N.C.; Chen, J.B.; Yang, K.H.; Wang, R.; Yu, X.H.; Dong, G.C.; Huang, X.F. The geology and mineralogy of the Beiya Skarn gold deposit in Yunnan, Southwest China. *Econ. Geol.* **2015**, *110*, 1625–1641. [CrossRef]

37. Xu, B.; Hou, Z.Q.; Griffin, W.L.; Lu, Y.; Belousova, E.; Xu, J.F.; O'Reilly, S.Y. Recycled volatiles determine fertility of porphyry deposits in collisional settings. *Am. Miner.* **2021**, *106*, 656–661. [CrossRef]

38. Xu, B.; Hou, Z.Q.; Griffin, W.L.; Zheng, Y.C.; Wang, T.; Guo, Z.; Hou, J.; Santosh, M.; O'Reilly, S.Y. Cenozoic lithospheric architecture and metallogenesis in Southeastern Tibet. *Earth-Sci. Rev.* **2021**, *214*, 103472. [CrossRef]

39. Wang, Z.X.; Zheng, Y.C.; Xu, B.; Hou, Z.Q.; Zhang, A.P.; Shen, Y.; Ma, R.; Wu, C.D.; Xu, P.Y. Hydrous Juvenile Lower Crust at the Western Yangtze Craton Margin as the Main Source of the Beiya Porphyry–skarn Au Deposit. *Acta Geol. Sin.-Engl. Ed.* **2021**, *96*, 972–992. [CrossRef]

40. Yang, Z.M.; Hou, Z.Q.; Xu, J.F.; Bian, X.F.; Wang, G.R.; Yang, Z.S.; Tian, S.H.; Liu, Y.C.; Wang, Z.L. Geology and origin of the post-collisional Narigongma porphyry Cu–Mo deposit, southern Qinghai, Tibet. *Gondwana Res.* **2014**, *26*, 536–556. [CrossRef]

41. Lin, B.; Wang, L.; Tang, J.; Song, Y.; Cao, H.; Baker, M.J.; Zhang, L.; Zhou, X. Geology, geochronology, geochemical characteristics and origin of Baomai porphyry Cu (Mo) deposit, Yulong Belt, Tibet. *Ore Geol. Rev.* **2018**, *92*, 186–204. [CrossRef]

42. Hou, Z.Q.; Zeng, P.S.; Gao, Y.F.; Du, A.D.; Fu, D.M. Himalayan Cu–Mo–Au mineralization in the eastern Indo–Asian collision zone: Constraints from Re–Os dating of molybdenite. *Miner. Depos.* **2006**, *41*, 33–45. [CrossRef]

43. Liang, H.Y.; Campbell, I.H.; Allen, C.; Sun, W.D.; Liu, C.Q.; Yu, H.X.; Xie, Y.W.; Zhang, Y.Q. Zircon Ce^{4+}/Ce^{3+} ratios and ages for Yulong ore-bearing porphyries in eastern Tibet. *Miner. Depos.* **2006**, *41*, 152–159. [CrossRef]

44. Xu, X.W.; Cai, X.P.; Xiao, Q.B.; Peter, S.G. Porphyry Cu–Au and associated polymetallic Fe–Cu–Au deposits in the Beiya Area, western Yunnan Province, south China. *Ore Geol. Rev.* **2007**, *31*, 224–246. [CrossRef]

45. He, W.Y.; Mo, X.X.; Yang, L.Q.; Xing, Y.L.; Dong, G.C.; Yang, Z.; Gao, X.; Bao, X.S. Origin of the Eocene porphyries and mafc microgranular enclaves from the Beiya porphyry Au polymetallic deposit, western Yunnan, China: Implications for magma mixing/mingling and mineralization. *Gondwana Res.* **2016**, *40*, 230–248. [CrossRef]

46. Li, W.C.; Wang, J.H.; He, Z.H.; Dou, S. Formation of Au-polymetallic ore deposits in alkaline porphyries at Beiya, Yunnan, Southwest China. *Ore Geol. Rev.* **2016**, *73*, 241–252. [CrossRef]

47. Xu, L.; Bi, X.; Hu, R.; Zhang, X.; Su, W.; Qu, W.; Hu, Z.; Tang, Y. Relationships between porphyry Cu–Mo mineralization in the Jinshajiang–Red River metallogenic belt and tectonic activity: Constraints from zircon U–Pb and molybdenite Re–Os geochronology. *Ore Geol. Rev.* **2012**, *48*, 460–473. [CrossRef]

48. Deng, J.; Wang, Q.F.; Li, G.J.; Hou, Z.Q.; Jiang, C.Z.; Danyushevsky, L. Geology and genesis of the giant Beiya porphyry–skarn gold deposit, northwestern Yangtze Block, China. *Ore Geol. Rev.* **2015**, *70*, 457–485. [CrossRef]

49. Tapponnier, P.; Lacassin, R.; Leloup, P.H.; Schärer, U.; Dalai, Z.; Haiwei, W.; Jiayou, Z. The Ailao Shan/Red River metamorphic belt: Tertiary left-lateral shear between Indochina and South China. *Nature* **1990**, *343*, 431–437. [CrossRef]

50. He, Z.H.; Wang, Y.; Mo, X.X.; Zeng, P.S.; Yu, X.H.; Liu, H.L. Sources of ore-forming materials in the Chang'an gold deposit, Yunnan province: Evidence from the contents of ore-forming elements in ore, strata and magma from ore district. *J. East China Inst. Technol. (Nat. Sci.)* **2008**, *31*, 207–212, (In Chinese with English abstract).

51. Zhang, J.; Wang, H.; Li, S.; Li, T. Paleogene magmatism and gold metallogeny of the Jinping terrane in the Ailaoshan ore belt, Sanjiang Tethyan Orogen (SW China): Geology, deposit type and tectonic setting. *Ore Geol. Rev.* **2017**, *91*, 620–637. [CrossRef]

52. Xu, L.L.; Bi, X.W.; Hu, R.Z.; Tang, Y.Y.; Wang, X.S.; Huang, M.L.; Wang, Y.J.; Ma, R.; Liu, G. Contrasting whole-rock and mineral compositions of ore-bearing (Tongchang) and ore-barren (Shilicun) granitic plutons in SW China: Implications for petrogenesis and ore genesis. *Lithos* **2019**, *336–337*, 54–66. [CrossRef]

53. Xu, L.; Bi, X.; Hu, R.; Tang, Y.; Wang, X.; Xu, Y. LA–ICP–MS mineral chemistry of titanite and the geological implications for exploration of porphyry Cu deposits in the Jinshajiang—Red River alkaline igneous belt, SW China. *Miner. Pet.* **2015**, *109*, 181–200. [CrossRef]

54. Xu, L.; Bi, X.; Hu, R.; Qi, Y.; Tang, Y.; Wang, X.; Zhu, J. Redox states and genesis of magmas associated with intra-continental porphyry Cu–Au mineralization within the Jinshajiang–Red River alkaline igneous belt, SW China. *Ore Geol. Rev.* **2015**, *73*, 330–345. [CrossRef]

55. Stock, M.; Humphreys, M.; Smith, V.C.; Isaia, R.; Pyle, M.J.S.D.M. Late-stage volatile saturation as a potential trigger for explosive volcanic eruptions. *Nat. Geosci.* **2016**, *9*, 249–254. [CrossRef]

56. Liu, Y.; Hu, Z.; Gao, S.; Günther, D.; Xu, J.; Gao, C.; Chen, H. In situ analysis of major and trace elements of anhydrous minerals by LA–ICP–MS without applying an internal standard. *Chem. Geol.* **2008**, *257*, 34–43. [CrossRef]

57. Chen, L.; Liu, Y.; Hu, Z.; Gao, S.; Zong, K.; Chen, H. Accurate determinations of fifty-four major and trace elements in carbonate by LA–ICP–MS using normalization strategy of bulk components as 100%. *Chem. Geol.* **2011**, *284*, 283–295. [CrossRef]

58. Deer, W.A.; Howie, R.A.; Zussman, J. *Sheet Silicates In Rock-Forming Minerals*; Wiley: Hoboken, NJ, USA, 1962; Volume 3C.

59. Li, X.; Zhang, C. Machine Learning Thermobarometry for Biotite-Bearing Magmas. *J. Geophys. Res. Solid Earth* **2022**, *127*, e2022JB024137. [CrossRef]

60. Zhang, C.; Li, X.; Behrens, H.; Holtz, F. Partitioning of OH–F–Cl between biotite and silicate melt: Experiments and an empirical model. *Geochim. Et Cosmochim. Acta* **2021**, *317*, 155–179. [CrossRef]

61. Giesting, P.; Filiberto, J. Quantitative models linking igneous amphibole composition with magma Cl and OH content. *Am. Miner.* **2014**, *99*, 852–865. [CrossRef]

62. Leake, B.E.; Woolley, A.R.; Arps, C.E.S.; Birch, W.D.; Gilbert, M.C.; Grice, J.D.; Hawthorne, F.; Kato, A.; Kisch, H.J.; Krivovichev, V.G.; et al. Nomenclature of Amphiboles; Report of the Subcommittee on Amphiboles of the International Mineralogical Association Commission on New Minerals and Mineral Names. *Miner. Mag.* **1997**, *61*, 295–310. [CrossRef]

63. Sato, H.; Holtz, F.; Behrens, H.; Botcharnikov, R.; Nakada, S. Experimental Petrology of the 1991–1995 Unzen Dacite, Japan. Part II: Cl/OH Partitioning between Hornblende and Melt and its Implications for the Origin of Oscillatory Zoning of Hornblende Phenocrysts. *J. Pet.* **2004**, *46*, 339–354. [CrossRef]

64. Eggler, D.H. Amphibole stability in H_2O-undersaturated calc-alkaline melts. *Earth Planet. Sci. Lett.* **1972**, *15*, 28–34. [CrossRef]

65. Allen, J.C.; Boettcher, A.L.; Marland, G. Amphiboles in andesite and basalt: I. Stability as a function of $PTfO_2$. *Am. Mineral. J. Earth Planet. Mater.* **1975**, *60*, 1069–1085.

66. Nandedkar, R.H.; Ulmer, P. Fractional crystallization of primitive, hydrous arc magmas: An experimental study at 0.7 GPa. *Contrib. Mineral. Petrol.* **2014**, *167*, 1015. [CrossRef]

67. Schmidt, M.W. Amphibole composition in tonalite as a function of pressure: An experimental calibration of the Al-in-hornblende barometer. *Contrib. Miner. Pet.* **1992**, *110*, 304–310. [CrossRef]

68. Molina, J.; Moreno, J.; Castro, A.; Rodríguez, C.; Fershtater, G. Calcic amphibole thermobarometry in metamorphic and igneous rocks: New calibrations based on plagioclase/amphibole Al–Si partitioning and amphibole/liquid Mg partitioning. *Lithos* **2015**, *232*, 286–305. [CrossRef]

69. Ridolfi, F.; Renzulli, A. Calcic amphiboles in calc-alkaline and alkaline magmas: Thermobarometric and chemometric empirical equations valid up to 1130 °C and 2.2 GPa. *Contrib. Mineral. Petrol.* **2012**, *163*, 877–895. [CrossRef]

70. Anderson, J.L.; Barth, A.P.; Wooden, J.L.; Mazdab, F. Thermometers and Thermobarometers in Granitic Systems. *Rev. Miner. Geochem.* **2008**, *69*, 121–142. [CrossRef]

71. Walker, B.A.; Klemetti, E.; Grunder, A.L.; Dilles, J.H.; Tepley, F.J.; Giles, D. Crystal reaming during the assembly, maturation, and waning of an eleven-million-year crustal magma cycle: Thermobarometry of the Aucanquilcha Volcanic Cluster. *Contrib. Miner. Pet.* **2013**, *165*, 663–682. [CrossRef]

72. Erdmann, S.; Martel, C.; Pichavant, M.; Kushnir, A.R.L. Amphibole as an archivist of magmatic crystallization conditions: Problems, potential, and implications for inferring magma storage prior to the paroxysmal 2010 eruption of Mount Merapi, Indonesia. *Contrib. Miner. Pet.* **2014**, *167*, 1016. [CrossRef]

73. Gorini, A.; Ridolfi, F.; Piscaglia, F.; Taussi, M.; Renzulli, A. Application and reliability of calcic amphibole thermobarometry as inferred from calc-alkaline products of active geothermal areas in the Andes. *J. Volcanol. Geotherm. Res.* **2018**, *358*, 58–76. [CrossRef]

74. Ferry, J.M.; Watson, E.B. New thermodynamic models and revised calibrations for the Ti-in-zircon and Zr-in-rutile thermometers. *Contrib. Miner. Pet.* **2007**, *154*, 429–437. [CrossRef]

75. Khedr, M.Z.; Zaghloul, H.; Takazawa, E.; El-Nahas, H.; Azer, M.K.; El-Shafei, S.A. Genesis and evaluation of heavy minerals in black sands: A case study from the southern Eastern Desert of Egypt. *Geochemistry* **2023**, *83*, 125945. [CrossRef]

76. Popa, R.G.; Tollan, P.; Bachmann, O.; Schenker, V.; Ellis, B.; Allaz, J.M. Water exsolution in the magma chamber favors effusive eruptions: Application of Cl–F partitioning behavior at the Nisyros–Yali volcanic area. *Chemical Geology* **2021**, *570*, 120170. [CrossRef]

77. Boynton, W.V. Cosmochemistry of the Rare Earth Elements: Meteorite Studies. In *Developments in Geochemistry*; Elsevier: Amsterdam, The Netherlands, 1984; Volume 2, pp. 63–114.

78. Defant, M.J.; Drummond, M.S. Derivation of some modern arc magmas by melting of young subducted lithosphere. *Nature* **1990**, *347*, 662–665. [CrossRef]

79. Moyen, J.F. High Sr/Y and La/Yb ratios: The meaning of the "adakitic signature". *Lithos* **2009**, *112*, 556–574. [CrossRef]

80. Pan, L.C.; Hu, R.Z.; Wang, X.S.; Bi, X.W.; Zhu, J.J.; Li, C. Apatite trace element and halogen compositions as petrogenetic–metallogenic indicators: Examples from four granite plutons in the Sanjiang region, SW China. *Lithos* **2016**, *254–255*, 118–130. [CrossRef]

81. Bruand, E.; Fowler, M.; Storey, C.; Laurent, O.; Antoine, C.; Guitreau, M.; Heilimo, E.; Nebel, O. Accessory mineral constraints on crustal evolution: Elemental fingerprints for magma discrimination. *Geochem. Perspect. Lett.* **2020**, *13*, 7–12. [CrossRef]

82. Sun, C.Y.; Cawood, P.A.; Xu, W.L.; Zhang, X.M.; Tang, J.; Li, Y.; Sun, Z.X.; Xu, T. In situ geochemical composition of apatite in granitoids from the eastern Central Asian Orogenic Belt: A window into petrogenesis. *Geochim. Et Cosmochim. Acta* **2021**, *317*, 552–573. [CrossRef]

83. Xu, L.L.; Zhu, J.J.; Huang, M.L.; Pan, L.C.; Hu, R.; Bi, X.W. Genesis of hydrous–oxidized parental magmas for porphyry Cu (Mo, Au) deposits in a postcollisional setting: Examples from the Sanjiang region, SW China. *Miner. Depos.* **2023**, *58*, 161–196. [CrossRef]

84. Zhao, X.; Yu, X.H.; Mo, X.X.; Zhang, J.; Liu, B.X. Petrological and geochemical characteristics of Cenozoic alkali-rich porphyries and xenoliths hosted in western Yunnan province. *Geoscience* **2009**, *18*, 217–228, (In Chinese with English abstract).

85. Samperton, K.M.; Schoene, B.; Cottle, J.M.; Keller, C.B.; Crowley, J.L.; Schmitz, M.D. Magma emplacement, differentiation and cooling in the middle crust: Integrated zircon geochronological–geochemical constraints from the Bergell Intrusion, Central Alps. *Chem. Geol.* **2015**, *417*, 322–340. [CrossRef]

86. Lee, R.; Dilles, J.H.; Tosdal, R.M.; Wooden, J.L.; Mazdab, F.K. Magmatic Evolution of Granodiorite Intrusions at the El Salvador Porphyry Copper Deposit, Chile, Based on Trace Element Composition and U/Pb Age of Zircons. *Econ. Geol.* **2017**, *112*, 245–273. [CrossRef]

87. Szymanowski, D.; Wotzlaw, J.-F.; Ellis, B.S.; Bachmann, O.; Guillong, M.; von Quadt, A. Protracted near-solidus storage and pre-eruptive rejuvenation of large magma reservoirs. *Nat. Geosci.* **2017**, *10*, 777–782. [CrossRef]

88. Ghiorso, M.S.; Gualda, G.A.R. An H_2O–CO_2 mixed fluid saturation model compatible with rhyolite-MELTS. *Contrib. Miner. Pet.* **2015**, *169*, 53. [CrossRef]

89. Collins, W.J.; Murphy, J.B.; Johnson, T.E.; Huang, H.Q. Critical role of water in the formation of continental crust. *Nat. Geosci.* **2020**, *13*, 331–338. [CrossRef]

90. Annen, C.; Blundy, J.D.; Sparks, R.S.J. The Genesis of Intermediate and Silicic Magmas in Deep Crustal Hot Zones. *J. Pet.* **2006**, *47*, 505–539. [CrossRef]

91. Christie, D.M.; Carmichael, I.S.; Langmuir, C.H. Oxidation states of mid-ocean ridge basalt glasses. *Earth Planet. Sci. Lett.* **1986**, *79*, 397–411. [CrossRef]

92. Mathez, E.A. Influence of degassing on oxidation-states of basalticmagmas. *Nature* **1984**, *310*, 371–375. [CrossRef]

93. Candela, P.A.; Holland, H.D. A mass transfer model for copper and molybdenum in magmatic hydrothermal systems; the origin of porphyry-type ore deposits. *Econ. Geol.* **1986**, *81*, 1–19. [CrossRef]

94. Lee, C.T.A.; Leeman, W.P.; Canil, D.; A Li, Z.X. Similar V/Sc Systematics in MORB and Arc Basalts: Implications for the Oxygen Fugacities of their Mantle Source Regions. *J. Pet.* **2005**, *46*, 2313–2336.

95. Burgisser, A.; Scaillet, B. Redox evolution of a degassing magma rising to the surface. *Nature* **2007**, *445*, 194–197. [CrossRef]

96. Kelley, K.A.; Cottrell, E. The influence of magmatic differentiation on the oxidation state of Fe in a basaltic arc magma. *Earth Planet. Sci. Lett.* **2012**, *329–330*, 109–121. [CrossRef]

97. de Moor, J.M.; Fischer, T.P.; Sharp, Z.D.; King, P.L.; Wilke, M.; Botcharnikov, R.E.; Cottrell, E.; Zelenski, M.; Marty, B.; Klimm, K.; et al. Sulfur degassing at Erta Ale (Ethiopia) and Masaya (Nicaragua) volcanoes: Implications for degassing processes and oxygen fugacities of basaltic systems. *Geochem. Geophys. Geosystems* **2013**, *14*, 4076–4108. [CrossRef]

98. Bell, A.S.; Simon, A. Experimental evidence for the alteration of the $Fe^{3+}/\Sigma Fe$ of silicate melt caused by the degassing of chlorine-bearing aqueous volatiles. *Geology* **2011**, *39*, 499–502. [CrossRef]

99. Park, J.W.; Campbell, I.H.; Chiaradia, M.; Hao, H.; Lee, C.T. Crustal magmatic controls on the formation of porphyry copper deposits. *Nat. Rev. Earth Environ.* **2021**, *2*, 542–557. [CrossRef]

100. Webster, J.D.; Goldoff, B.; Sintoni, M.F.; Shimizu, N.; De Vivo, B. C–O–H–Cl–S–F volatile solubilities, partitioning, and mixing in phonolitic–trachytic melts and aqueous–carbonic vapor ± saline liquid at 200 MPa. *J. Petrol.* **2014**, *55*, 2217–2248. [CrossRef]

101. Zajacz, Z.; Candela, P.A.; Piccoli, P.M.; Sanchez-Valle, C. The partitioning of sulfur and chlorine between andesite melts and magmatic volatiles and the exchange coefficients of major cations. *Geochim. Et Cosmochim. Acta* **2012**, *89*, 81–101. [CrossRef]

102. Heinrich, C.; Günther, D.; Audétat, A.; Ulrich, T.; Frischknecht, R. Metal fractionation between magmatic brine and vapor, determined by microanalysis of fluid inclusions. *Geology* **1999**, *27*, 755–758. [CrossRef]